Majorana fermions of a two-dimensional p_x+ip_y superconductor

Yaacov E. Kraus,[1] Assa Auerbach,[2] H. A. Fertig,[3] and Steven H. Simon[4]
[1]*Department of Condensed Matter Physics, Weizmann Institute of Science, Rehovot 76100, Israel*
[2]*Department of Physics, Technion, Haifa 32000, Israel*
[3]*Department of Physics, Indiana University, Bloomington, Indiana 47405, USA*
[4]*Rudolf Peierls Centre for Theoretical Physics, University of Oxford, Oxford OX1 3NP, United Kingdom*
(Received 19 January 2009; revised manuscript received 11 March 2009; published 16 April 2009)

To investigate Majorana fermionic excitations of a p_x+ip_y superconductor, the Bogoliubov–de Gennes equation is solved on a sphere for two cases: (i) a vortex-antivortex pair at opposite poles and (ii) an edge near the south pole and an antivortex at the north pole. The vortex cores support a state of two Majorana fermions, the energy of which decreases exponentially with the radius of the sphere, independently of a moderate disorder potential. The tunneling conductance of an electron into the superconductor near the position of a vortex is computed for finite temperature and is compared to the case of an *s*-wave superconductor. The zero-bias conductance peak of the antivortex is half that of the vortex. This effect can be used as a probe of the order-parameter symmetry and as a direct measurement of the Majorana fermion.

DOI: 10.1103/PhysRevB.79.134515 PACS number(s): 74.50.+r, 03.67.Lx, 71.10.Pm, 74.20.Rp

I. INTRODUCTION

In the last few years it has appeared increasingly likely that nontrivial (or non-Abelian) topological phases of matter[1] may be produced in the laboratory. In fact, it is quite possible that these phases of matter have been produced although current experiments still leave room for doubt. Interest in such phases of matter is driven to a large extent by their possible application for building naturally error resistant, so-called "topological" quantum computers.[1] Among such topological phases of matter, perhaps the simplest is of the "Ising" or $SU(2)_2$ class,[1] which correspond to chiral p_x+ip_y BCS-paired superconductors.[2]

There are several possible physical systems where p_x+ip_y pairing is believed to be realized, including the *A* phase of superfluid ^{3}He (Ref. 3) (^{3}He*A*), the exotic superconductor Sr_2RuO_4,[4] and the $\nu=5/2$ quantum Hall state.[5,6] In addition, there have been recent proposals to realize p_x+ip_y pairing in cold fermion gases.[7] For quantum information processing applications, two dimensionality (or at least quasi-two-dimensionality) is necessary. This is certainly the case in quantum Hall systems and may also be achievable for Sr_2RuO_4 (which is a layered structure), for ^{3}He*A* films, and also potentially in cold atomic systems. For the purpose of this paper we will assume quasi-two-dimensionality, although some parts of our results are more general.

In these (weak coupling) p_x+ip_y systems, certain types of vortices (quasiparticles in the quantum Hall context[8]) are believed to carry zero energy Majorana fermions,[8,9] which are topologically protected degrees of freedom. In Sr_2RuO_4 and ^{3}He*A* the vortices that carry the Majorana fermions are the so-called half-quantum vortices, which can be thought of as a vortex in the order parameter of one spin species, without a vortex of the opposite species.[10] (Note that in spin-polarized p_x+ip_y systems, including proposed atomic gas realizations or the 5/2 state, there is no half-quantum vortex and the full quantum vortex carries the Majorana fermion).

A Majorana fermion is an operator which satisfies the fermionic anticommutation relation $\{\eta^\dagger(\boldsymbol{x}),\eta(\boldsymbol{x}')\}=2\delta(\boldsymbol{x}-\boldsymbol{x}')$, but equals to its own Hermitian conjugate $\eta\dagger=\eta$. Therefore $\eta^2=\eta^{\dagger 2}=\eta^\dagger\eta=1$. A fermion occupation number state can be defined as a linear combination of two Majorana fermions localized in two distinctive vortices $\psi(\boldsymbol{x})=[\eta_i(\boldsymbol{x})+i\eta_j(\boldsymbol{x})]/\sqrt{2}$ and $\psi^\dagger(\boldsymbol{x})=[\eta_i(\boldsymbol{x})-i\eta_j(\boldsymbol{x})]/\sqrt{2}$. This operator satisfies the usual fermionic relations $\{\psi^\dagger(\boldsymbol{x}),\psi(\boldsymbol{x}')\}=\delta(\boldsymbol{x}-\boldsymbol{x}')$ and $\psi^{\dagger 2}=\psi^2=0$. We shall call such a fermionic occupation number state a Majorana state. The energy of the Majorana state reflects the exponentially small hybridization between the wave functions of the two localized Majorana fermions.

The zero energy of the Majorana fermion in a single vortex is believed to be topologically protected against weak disorder.[8] But in the case of more than one vortex, an experimentally relevant question is whether the exponential localization and hybridization of the Majorana state is a property only of a clean system or is it robust against the inclusion of disorder. We find that these properties survive even in the presence of a moderate disorder.

Another unique property of the p_x+ip_y order parameter is the existence of low-energy chiral states, which are localized along the edge of the sample.[8] If a single vortex is present, the Majorana state is split between the vortex core and the edge.

Let us suppose that in one of the above systems, the relevant Majorana-fermion-carrying vortex has been created.[11] An important next step would be to design an experiment to demonstrate that the Majorana fermion is present in such a vortex.[12] In the case of Sr_2RuO_4, one obvious experiment would be an energy-resolved tunneling experiment, which measures the local density of states (LDOS).[13] An observation of a localized mode at precisely zero energy would be direct evidence of the Majorana fermion. For cold atoms, an analogous experiment for observing the LDOS would be an energy-resolved local particle annihilation experiment. For the other realizations of p_x+ip_y order it is not as clear how such an experiment would be performed.[14]

In principle such tunneling experiments could provide definitive evidence for the Majorana fermion. However, in

practice they may be prohibitively difficult. In the vortex, there will exist subgap bound states in the core known as Caroli-de-Gennes-Matricon (CdGM) states.[15,16] The spacing between the CdGM states is approximately $\epsilon_c=\Delta_0^2/\epsilon_F$, where Δ_0 is the gap (presumably on order of the critical temperature) and ϵ_F is the Fermi energy. Since the experimentally observed tunneling spectrum will be smeared by the temperature, this tunneling experiment would naively only have a clear signature for $T<\epsilon_c$. Unfortunately such low temperatures could potentially be unattainable in any of the proposed realizations ($\epsilon_c\approx 7$ μK in ^{3}He*A* and <0.1 mK in Sr_2RuO_4).

We find that within the reachable temperature region, $\epsilon_c<T<\Delta_0$, the central peak of the smeared LDOS of the antivortex is half the height of the peak of the vortex. We shall see that this distinction is clear evidence of the p_x+ip_y symmetry of the order parameter and of the existence of the Majorana fermion.

Generally speaking, a physical asymmetry between a vortex and an antivortex can occur only in superconductors which break time-reversal symmetry, such as p_x+ip_y superconductors.[17] The order parameter of such superconductors involves internal angular momentum, which is interlaced with the angular momentum of the vortex according to theirs relative directions.[18]

This paper is organized as follows:

In Sec. II we implement the p_x+ip_y superconductor on a sphere, with vortex-antivortex pair at the poles.[19] Using monopole harmonics functions, we numerically solve the Bogoliubov–de Gennes (BdG) equation, and get the full BdG spectrum.

In Sec. III we test the exponential decay of the Majorana state energy as a function of the distance between the vortices in the presence of disorder. We find it is unaffected even in the presence of a moderate disorder.

In Sec. IV we put an edge around the south pole of the sphere and observe the edge excitations and their linear dispersion. In Sec. V we calculate the tunneling conductance of an electron into the superconductor near the position of a vortex or an antivortex at zero temperature and at elevated temperature. We find an asymmetry effect in the zero-bias conductance between the vortex and the antivortex, which one can use as "smoking gun" evidence of the existence of the Majorana fermion. We compare it to the tunneling spectrum for a regular *s*-wave superconductor to support this conclusion. Our analysis shows that this effect will occur for any spin-polarized chiral superconductor (chiral-*p*, chiral-*d*,…). However, it occurs for the single vortex only for the chiral-*p* case, whereas it occurs for the double vortex for chiral-*d* and correspondingly higher vortices for higher pairing symmetries. Some of the results of this paper were recently published in a short format.[20]

II. BdG THEORY ON A SPHERE

Consider a two-dimensional uniform p_x+ip_y superconductor of spinless fermions. The excitation spectrum is given by the BdG equation[21]

$$\begin{pmatrix} \hat{T}-\epsilon_F+W & \Delta \\ \Delta^\dagger & -(\hat{T}-\epsilon_F+W) \end{pmatrix}\begin{pmatrix} u_n \\ v_n \end{pmatrix}=E_n\begin{pmatrix} u_n \\ v_n \end{pmatrix}, \quad (1)$$

where $\hat{T}$ is the kinetic-energy operator and ϵ_F is the Fermi energy. W denotes electrostatic potential and will be zero in this section. Δ is the order-parameter field, which according to the p_x+ip_y symmetry is of the form

$$\Delta(\boldsymbol{x}-\boldsymbol{x}')=\Delta_0\frac{\partial_x+i\partial_y}{ik_F}\frac{1}{4\pi\xi_p^2}e^{-(\boldsymbol{x}-\boldsymbol{x}')^2/4\xi_p^2}$$
$$=\frac{\Delta_0}{8\pi i\xi_p^4 k_F}[(x-x')+i(y-y')]e^{-(\boldsymbol{x}-\boldsymbol{x}')^2/4\xi_p^2}. \quad (2)$$

Here Δ_0 is the pairing amplitude and k_F is the Fermi wave vector given by $\epsilon_F=k_F^2/2m^*$, where m^* is the electron effective mass. ξ_p is the pairing range, which is usually taken to be zero for simplicity, whereas in quantum Hall systems it is comparable to the magnetic length. In Fourier space,

$$\Delta_{\mathbf{k}}=\Delta_0\frac{k_x+ik_y}{k_F}e^{-k^2\xi_p^2}, \quad (3)$$

which shows that Δ_0 is approximately the energy gap. Although we have written down a special case of p_x+ip_y order parameter, the $\mathbf{k}\to 0$ part is universal.

All the calculations in this paper are considered to be in the short-range pairing limit, where $k_F\xi_p\ll 1$. However, the form Eq. (3) remains acceptable up to $k_F\xi_p\approx 1$, although due to the exponential factor the amplitude is highly reduced (but can be compensated by multiplying by a factor of $e^{k_F^2\xi_p^2}$). We have checked that none of our results change substantially even for $k_F\xi_p\approx 1$.

A vortex (+) and an antivortex (−) are described by the order parameters

$$\Delta_\pm(\boldsymbol{x},\boldsymbol{x}')=\Delta(\boldsymbol{x}-\boldsymbol{x}')f_v(\bar{r}/\xi)e^{\pm i\bar{\phi}}, \quad (4)$$

where $\bar{r},\bar{\phi}$ denote the polar coordinates of the pair center of mass $(\boldsymbol{x}+\boldsymbol{x}')/2$. The amplitude profile of the vortex $f_v(x)$ vanishes at the origin and approaches unity at $x\gg 1$. ξ is Pippard's coherence length,[22]

$$\xi=\frac{2\epsilon_F}{\pi\Delta_0 k_F}. \quad (5)$$

Note that for the vortex Δ_+, the relative and the center-of-mass angular momenta are aligned, while for the antivortex Δ_-, they have opposite chirality.

We implement the BdG equation on a sphere of radius R, parameterized by the unit vector $\boldsymbol{\Omega}=(\theta,\phi)$. The spherical geometry has two important advantages: (i) it has no boundaries, which strongly affect the low-energy spectrum (as will be discussed in Sec. IV) and (ii) it enables the use of monopole harmonics functions as a basis, which appears to be very convenient for the p_x+ip_y pairing. However, the spherical symmetry forces us to consider an antipodal vortex-antivortex pair. We set such a vortex-antivortex pair in the north and south poles, respectively, see Fig. 1. The azimuthal

symmetry of this configuration conserves the azimuthal angular momentum, which greatly reduces the computational difficulty of the BdG diagonalization.

The spherical geometry is used in this paper for calculations on finite-size geometry, where the physical limit of far separated vortex-antivortex pair in the two-dimensional plane is approached in the $R\to\infty$ limit. Since the quantities we are interested in will be found to decay exponentially fast with R/ξ, our finite sphere calculations will be relevant at values of R/ξ which are not enormously large, i.e., in moderate vortices density. Of course, our calculations would be even more directly relevant to thin spherical shells which might be experimentally created on small spherical substrates.

The order-parameter field on the sphere is taken to be of the following form:[23]

$$\Delta_V(\mathbf{\Omega},\mathbf{\Omega}') = \Delta_p(\mathbf{\Omega},\mathbf{\Omega}')F_V(\overline{\mathbf{\Omega}}), \tag{6}$$

$$\Delta_p(\mathbf{\Omega},\mathbf{\Omega}') = \frac{\Delta_0}{(4\pi\xi_p^2)\left(l_F+\frac{1}{2}\right)} \times (\alpha\beta'-\beta\alpha')\left|\alpha\alpha'^{*}+\beta\beta'^{*}\right|^{2(R/\xi_p)^2},$$

$$\alpha = \cos(\theta/2), \tag{7}$$

$$\beta = \sin(\theta/2)e^{-i\phi}. \tag{8}$$

where Δ_p gives the pairing of the particles and is constructed by the spinor functions α and β. The $(\cdots)$ factor in Δ_p acquires a 2π phase winding when $\mathbf{\Omega}$ encircles $\mathbf{\Omega}'$, which describes p_x+ip_y pairing. The $|\cdots|$ factor keeps the particles within relative distance ξ_p. l_F is the Fermi angular momentum given by

$$\epsilon_F = \frac{l_F(l_F+1)}{2mR^2}. \tag{9}$$

In this way Δ_p reproduces Δ [Eq. (2)] in the large R limit.

$F_V(\overline{\mathbf{\Omega}})$ describes the vorticity of the pair center of mass $\overline{\mathbf{\Omega}}=(\mathbf{\Omega}+\mathbf{\Omega}')/2$. We choose F_V to describe an antivortex on the north pole and a vortex on the south pole depicted in Fig. 1. For the vortex pair field, we use (without self-consistency) the approximate solution of the Gross-Pitaevskii equation of a vortex[24]

$$F_V(\mathbf{\Omega}) = \frac{\sin\theta(R/\xi)}{\sqrt{1+[\sin\theta(R/\xi)]^2}}e^{i\phi}, \tag{10}$$

with $\xi_p<\xi\ll R$ for simplicity.

We expand the order parameter as a series of monopole harmonics[25] Y_{qlm} of $q=-\frac{1}{2}$, and l,m half integers.[8,23] These monopole harmonics represent eigenstates of a particle on a sphere in a radial magnetic field with $2q=-1$ flux quanta penetrating into the sphere (the $-$ sign was chosen for correspondence with the composite fermion picture of the $\nu=5/2$ state). In this basis, the BdG equation is represented as a matrix,

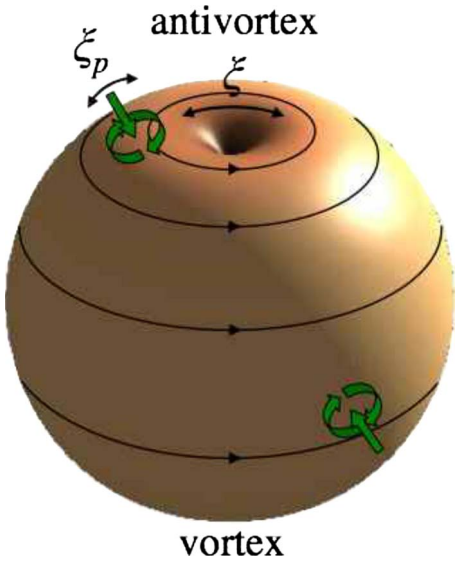

FIG. 1. (Color online) A vortex-antivortex pair of the p_x+ip_y superconductor on the sphere, described by Eq. (6). Thin black lines represent the current flow. Wide green arrows represent the pair relative angular momentum. ξ_p is the pairing range. ξ is the coherence length, which determines the vortex core size.

$$\begin{pmatrix} T_{lm,l'm'} & \Delta^V_{lm,\bar{l}'\bar{m}'} \\ (\Delta^{V\dagger})_{\bar{l}\bar{m},l'm'} & -T_{\bar{l}\bar{m},\bar{l}'\bar{m}'} \end{pmatrix}\begin{pmatrix} u_{n,l'm'} \\ v_{n,\bar{l}'\bar{m}'} \end{pmatrix} = E_n\begin{pmatrix} u_{n,lm} \\ v_{n,\bar{l}\bar{m}} \end{pmatrix}, \tag{11}$$

with summation over primed indices and with the following matrix elements:

$$T_{lm,l'm'} = \delta_{ll'}\delta_{mm'}\epsilon_F\left(\frac{l(l+1)-\frac{1}{4}}{l_F(l_F+1)-\frac{1}{4}}-1\right), \tag{12}$$

$$\Delta^V_{lm,l'm'} = \delta_{m',1-m}\Delta_0\sqrt{\frac{1}{16\pi}(2l+1)(2l'+1)} \times[D_l+(-1)^{l+l'}D_{l'}]\sum_L\sqrt{2L+1}f^V_L \times\begin{pmatrix} l & l' & L \\ \frac{1}{2} & -\frac{1}{2} & 0 \end{pmatrix}\begin{pmatrix} l & l' & L \\ -m & m-1 & 1 \end{pmatrix}, \tag{13}$$

$$D_l \approx \frac{l}{l_F}e^{-l^2(\xi_p/R)^2}. \tag{14}$$

The matrix element $\Delta^V_{lm,l'm'}$ [Eqs. (13) and (14)] is justified in Appendix A. (A definition for f^V_L can also be found there.) As expected by the azimuthal symmetry, m is a good quantum number. This dramatically simplifies the numerics since the BdG matrix can be diagonalized for each m separately.

Diagonalizing Eq. (11) for each m produces a set of energies $E_{n,m}$ and corresponding eigenvectors $u_{n,lm}, v_{n,lm}$. The resultant BdG wave functions on the sphere are

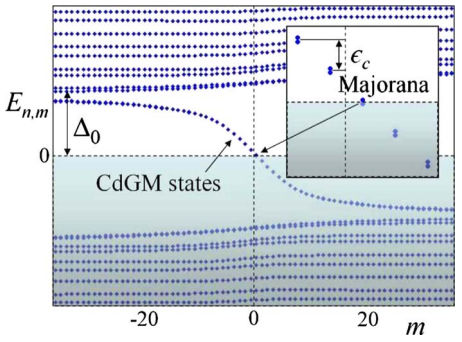

FIG. 2. (Color online) BdG spectrum $E_{n,m}$, of the vortex pair on the sphere, depicting the CdGM core states. The inset shows that their double degeneracies are split by weak tunneling between the poles. The positive energy member of the doublet, which saddles zero energy at $m=\frac{1}{2}$, is the Majorana state shared by the vortex and antivortex.

$$u_{n,m}(\mathbf{\Omega}) = \sum_l u_{n,lm} Y_{-1/2,l,m}(\mathbf{\Omega}) \tag{15}$$

$$v_{n,m}(\mathbf{\Omega}) = \sum_l v_{n,lm} Y^*_{-1/2,l,-m+1}(\mathbf{\Omega}). \tag{16}$$

In Fig. 2 we depict the BdG spectrum of the vortex pair state as a function of m. The spectrum shows an expected symmetry of the BdG equation, which implies that for every eigenvector (u_n, v_n) with energy E_n, the vector (v_n^*, u_n^*) is also an eigenvector with energy $-E_n$. Hence according to Eqs. (15) and (16),

$$u_{n,m} = (v_{n',-m+1})^*,$$

$$E_{n,m} = -E_{n',-m+1}. \tag{17}$$

The continuum states above the gap $|E_n| > \Delta_0$ are extended, while the branch that approaches zero is the $p_x + ip_y$ version of the CdGM core states. Their dispersion is

$$E_m^c \approx \left(\frac{1}{2} - m\right)\epsilon_c,$$

$$\epsilon_c = \Delta_0^2/\epsilon_F, \tag{18}$$

and their number is of order ϵ_F/Δ_0.[16]

As seen in the inset of Fig. 2, each CdGM state is almost doubly degenerate. The splitting represents weak tunneling between the north and south pole cores and decreases exponentially with the radius of the sphere $\delta E_m^c \sim e^{-R/\xi}$ for $R \gg \xi$. In particular, the lowest positive energy E_{0^+}, and its negative companion E_{0^-} (both at $m=\frac{1}{2}$), approach zero as $e^{-R/\xi}$, is shown in Fig. 3. The probability densities $|u_{0^+}(\theta)|^2 = |v_{0^-}(\theta)|^2$ and $|u_{0^-}(\theta)|^2 = |v_{0^+}(\theta)|^2$ are depicted in Fig. 4. The wave functions are symmetric and antisymmetric superpositions of the north and south localized core states.

In the infinite sphere limit $E_{0^+} \approx E_{0^-} \approx 0$, and the wave functions $u_0(\mathbf{\Omega}) \approx v_0(\mathbf{\Omega})$ are equally split between the north and south poles. The corresponding BdG quasiparticle field operator near each pole $\eta(\mathbf{\Omega}) = u_0(\mathbf{\Omega})\psi(\mathbf{\Omega}) + v_0(\mathbf{\Omega})\psi^\dagger(\mathbf{\Omega})$, is

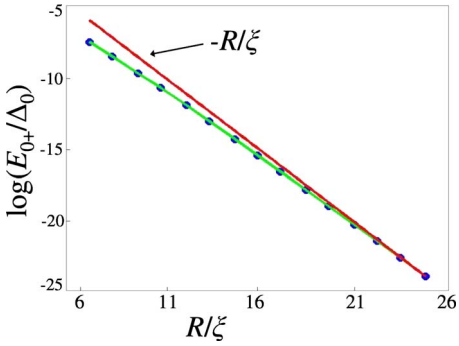

FIG. 3. (Color online) Energy of Majorana state E_{0^+} as a function of sphere radius R. The exponentially decreasing energy indicates tunnel splitting between vortex and antivortex core states.

a *Majorana fermion* operator $\eta \approx \eta^\dagger$.

The asymptotic behavior of the wave functions $u_0(r)$ in the plane are[7,16]

$$u_0(\boldsymbol{x}) \sim \begin{cases} J_0(k_F r) e^{-1/\pi \int^r d(r'/\xi) f_v(r'/\xi)} & \text{antivortex} \\ J_1(k_F r) e^{-1/\pi \int^r d(r'/\xi) f_v(r'/\xi)} e^{i\phi} & \text{vortex,} \end{cases} \tag{19}$$

where f_v was defined in Eq. (4). We confirmed this asymptotic behavior, as seen in Fig. 5.

The physical reason behind the difference in Eq. (19) between the vortex and the antivortex is that the phase winding of the order parameter is determined by the sum of the vorticity and the relative angular momentum. For a vortex the vorticity and the angular momentum are aligned, which yields the phase winding $e^{2i\phi}$. In that case the condition for Majorana fermion solution of the BdG equation, $u(\boldsymbol{x}) = v^*(\boldsymbol{x})$, can be fulfilled only by $u_0(\boldsymbol{x}) = \tilde{u}_0(r)e^{i\phi}$, where $\tilde{u}_0(r)$ vanishes at the origin [the $J_1(r)$ behavior is expected due to the azimuthal angular momentum 1]. By contrast, for an antivortex the order parameter is real since the vorticity and the relative angular momentum cancel each other. Thus the Majorana fermion solution is real and radial $u_0(\boldsymbol{x}) = \tilde{u}_0(r)$ and can be finite at the origin. [Here, $J_0(r)$ is ex-

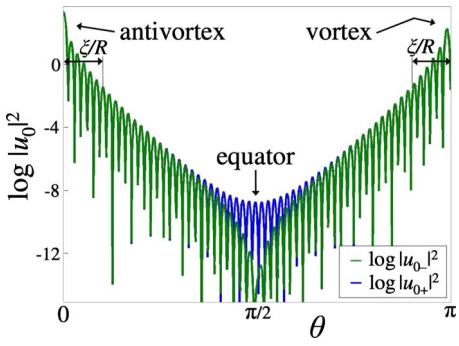

FIG. 4. (Color online) Probability densities of Majorana states $|u_0|^2$ versus latitude on the sphere θ. The smooth parts of the Majorana state wave functions $u_{0^+}(\theta)$ and $u_{0^-}(\theta)$ are approximately symmetric and antisymmetric with respect to reflection about the equator $\theta = \pi/2$. Both $|u_{0^+}|^2$ (blue) and $|u_{0^-}|^2$ (green) show the exponential localization in the (anti)vortex cores.

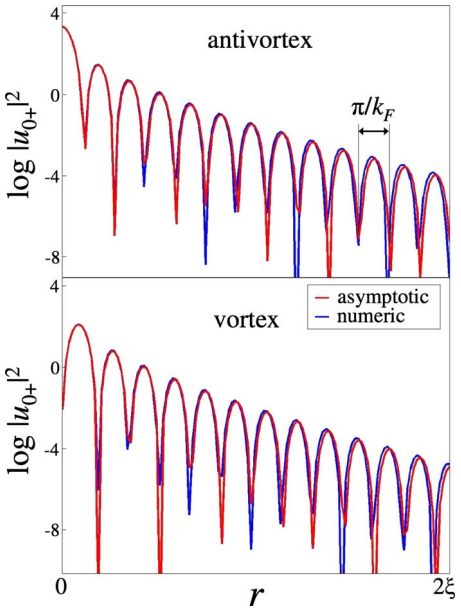

FIG. 5. (Color online) Probability distributions of Majorana state $|u_{0+}|^2$ as a function of the distance from the (anti)vortex center r, at the cores vicinities. The wave functions have exponentially small weights near the equator. The asymptotic (red) and the numeric (blue) wave functions show excellent agreement.

pected, since the angular momentum is zero.] We will see in Sec. V that this difference is crucial for an experimental signature of the Majorana state.

The excellent agreement between the asymptotic and numerical wave functions, as seen in Fig. 5, reveals the underlying physics of the core states. The radial profile of the order parameter serves only as a confinement and therefore determines only the exponential decay of the wave function (and very weakly the spacing between the core states). The short-range part of the wave function is controlled by a Bessel function, which is determined only by the symmetry and the total angular momentum. Furthermore, the specific pairing functions and pairing range do not play any apparent role.

s -wave. In order to emphasize the unique behavior of the chiral p-wave order parameter, we compare it to a regular s-wave order parameter characterized with the same set of physical parameters. An order parameter with s-wave symmetry in a plane, in the presence of a vortex, will have the form

$$\Delta^S_{\pm}(\boldsymbol{x},\boldsymbol{x}') = \Delta^S(\boldsymbol{x}-\boldsymbol{x}')f_v(\bar{r}/\xi)e^{\pm i\bar{\phi}}, \tag{20}$$

$$\Delta^S(\boldsymbol{x}-\boldsymbol{x}') = \Delta_0\frac{1}{4\pi\xi_p^2}e^{-(\boldsymbol{x}-\boldsymbol{x}')^2/4\xi_p^2}, \tag{21}$$

where f_v is the same as in Eq. (4). Δ^S provides the s-wave pairing, with the same pairing range ξ_p of the p_x+ip_y order parameter.

Implementing the order parameter on a sphere with a vortex-antivortex pair at the poles is quite similar to the p_x+ip_y case:

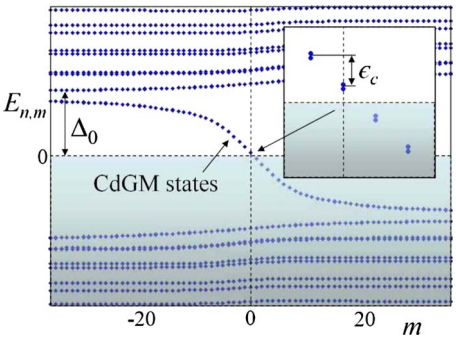

FIG. 6. (Color online) The BdG spectrum $E_{n,m}$, of an s-wave superconductor, with the same physical parameters of the p_x+ip_y in Fig. 2. The distinction from the p_x+ip_y case can be noticed in the inset, where the energies of the CdGM states are shifted by half the level spacing, therefore lacking a Majorana state which saddles zero energy.

$$\Delta^S_V(\boldsymbol{\Omega},\boldsymbol{\Omega}') = \Delta^S_p(\boldsymbol{\Omega},\boldsymbol{\Omega}')F_V(\overline{\boldsymbol{\Omega}}), \tag{22}$$

$$\Delta^S_p(\boldsymbol{\Omega},\boldsymbol{\Omega}') = \frac{\Delta_0}{4\pi\xi_p^2}|\alpha\alpha'^* + \beta\beta'^*|^{2(R/\xi_p)^2}, \tag{23}$$

where F_V is unchanged.

Without the chirality, the order parameter can be expanded in the regular spherical harmonics Y_{lm} basis, with l,m integers. In this basis, the matrix forms of the kinetic term and the order parameter are

$$T_{lm,l'm'} = \delta_{ll'}\delta_{mm'}\epsilon_F\left(\frac{l(l+1)}{l_F(l_F+1)}+1\right), \tag{24}$$

$$\begin{aligned}\Delta^S_{lm,l'm'} = &-\delta_{m',1-m}\Delta_0\sqrt{\frac{1}{16\pi}(2l+1)(2l'+1)}\\ &\times(D^S_l + D^S_{l'})\sum_L\sqrt{2L+1}f^V_L\begin{pmatrix} l & l' & L\\ 0 & 0 & 0\end{pmatrix}\\ &\times\begin{pmatrix} l & l' & L\\ -m & m-1 & 1\end{pmatrix},\end{aligned} \tag{25}$$

$$D^S_l \approx e^{-l^2(\xi_p/R)^2}. \tag{26}$$

Our method of computing $\Delta^S_{lm,l'm'}$ is almost the same as that for $\Delta_{lm,l'm'}$ (Appendix A) but with q set to 0 and integer l,m. D^S_l is given essentially by Eq. (A7) and is approximated in a way analogous to D_l [Eq. (14)] but without the chirality factor l/l_F.

The BdG spectrum of the s-wave system is generally similar to that of the p_x+ip_y system, as seen in Fig. 6, which was plotted with the same parameters that were used to plot Fig. 2. Both the extended states, with $|E_n|>\Delta_0$, and the CdGM states, with $E^c_m \approx (\frac{1}{2}-m)\epsilon_c$, are present. Here m is an integer, the energies of the CdGM states are shifted by $\frac{1}{2}\epsilon_c$ compared to the p_x+ip_y case, and the Majorana state is absent.

Far from the vortex core, the s-wave and the p_x+ip_y show almost the same gapped spectrum. Fourier transforming the

BdG equation in the plane [Eqs. (1), (2), and (21); see Eq. (3)], and diagonalizing the BdG matrix gives

$$E_{\mathbf{k}}^{p_x+ip_y} = \sqrt{(k^2/2m^* - \epsilon_F)^2 + \left(\Delta_0 \frac{k}{k_F} e^{-k^2\xi_p^2}\right)^2}, \quad (27)$$

$$E_{\mathbf{k}}^{S} = \sqrt{(k^2/2m^* - \epsilon_F)^2 + (\Delta_0 e^{-k^2\xi_p^2})^2}, \quad (28)$$

where $k=(k_x^2+k_y^2)^{1/2}$.

The small difference between the two cannot be distinguished in a tunneling experiment. Nevertheless, the disparity in the CdGM states, and especially the existence of the Majorana state, may be observed by taking a difference in the tunneling LDOS, as we will see in Sec. V.

The last point to be mentioned is the insensitivity of the above results to the choice of Hamiltonian parameters. According to Eqs. (12)–(14) there are three free-dimensionless physical parameters: Δ_0/ϵ_F, l_F, and ξ_p/R, while ξ/R is determined by $l_F\Delta_0/\epsilon_F$ [according to Eq. (5)]. However, the asymptotic wave function [Eq. (19)] implies that the exponential envelope is controlled by ξ. Moreover, the energy of the Majorana state is also determined by ξ. We confirmed this numerically for the physical regime $\Delta_0 \ll \epsilon_F$. k_F, which is approximately $l_F R$, controls the oscillation frequency of the wave function, as seen in Eq. (19). The gap Δ_0 and ϵ_F determine the energy spacing of the core states ϵ_c and their number. ξ_p has negligible effect, up to $k_F\xi_p \leq 2\pi$, meaning that the pairing range has no significant effect either on the wave functions or on the energies of the core states. Additionally, modifying the vortex profile of Eq. (10)—to, for example, $\tanh[\sin\theta(R/\xi)]$—only modifies the wave functions slightly inside the cores, according to Eq. (19).

III. DISORDER

Disorder mixes states with different angular momentum m, thus making the BdG equation extremely hard to solve analytically. We study numerically the effect of disorder on the Majorana state by the addition of a white-noise random real potential to the BdG equation [Eq. (1)] given by

$$W(\mathbf{\Omega}) = \sum_{l,m}^{l_\Lambda} w_{lm} Y_{lm}(\mathbf{\Omega}), \quad (29)$$

where the w_{lm}'s are independently identically distributed, with $w_{l-m}=(-1)^m w_{lm}^*$. l_Λ is an ultraviolet cutoff. We want the potential to be independent of the radius of the sphere via l_Λ, therefore we take the real and imaginary parts of w_{lm} to be uniformly distributed in the interval $[-\frac{\sqrt{6\pi}W_0}{l_\Lambda}, \frac{\sqrt{6\pi}W_0}{l_\Lambda}]$, where W_0 is given in units of energy. This gives

$$\langle W^2(\mathbf{\Omega})\rangle = W_0^2, \quad (30)$$

as shown in Appendix B and demonstrated in Fig. 7.

The disorder breaks the azimuthal symmetry so that m is no longer a good quantum number. The matrix elements of $W(\mathbf{\Omega})$ are

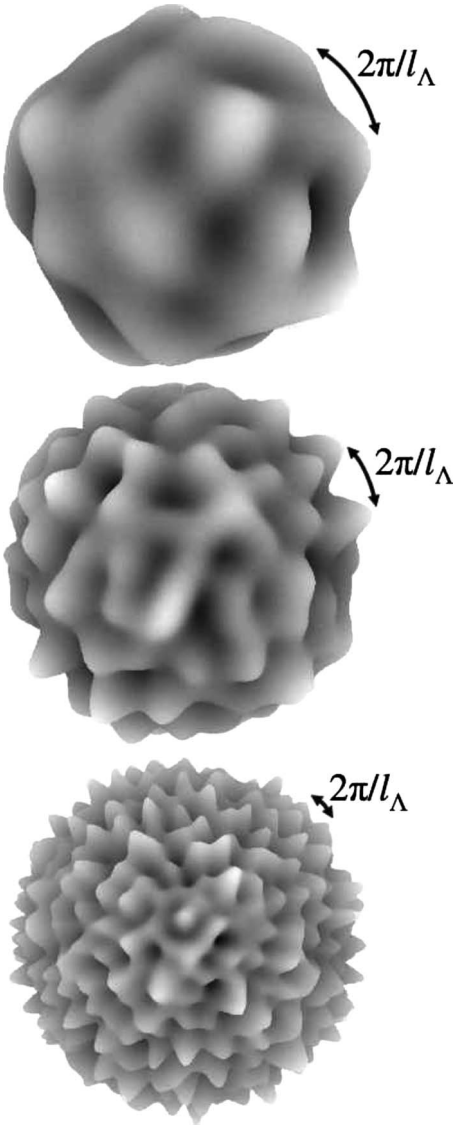

FIG. 7. Three white-noise potentials $W(\mathbf{\Omega})$ on the sphere, taken from the same distribution of harmonics components w_{lm} but of increasing high angular momentum cutoff l_Λ (from top to bottom). Each time l_Λ is multiplied by 2, while the disorder strength W_0 remains constant.

$$W_{lm,l'm'} = (-1)^{m-1/2}\sqrt{\frac{1}{4\pi}(2l+1)(2l'+1)} \times \sum_L^{l_\Lambda} \sqrt{2L+1} w_{L,m'-m} \begin{pmatrix} l & l' & L \\ \frac{1}{2} & -\frac{1}{2} & 0 \end{pmatrix} \times \begin{pmatrix} l & l' & L \\ m & -m' & m'-m \end{pmatrix}, \quad (31)$$

as derived in Appendix B.

Figure 8 depicts the disorder averaged energy of the Majorana state E_{0^+} versus R for increasing W_0. It can be seen that both the average energy (solid) and the standard deviation (error bars) decay exponentially in the regime $W_0 < \epsilon_F$.

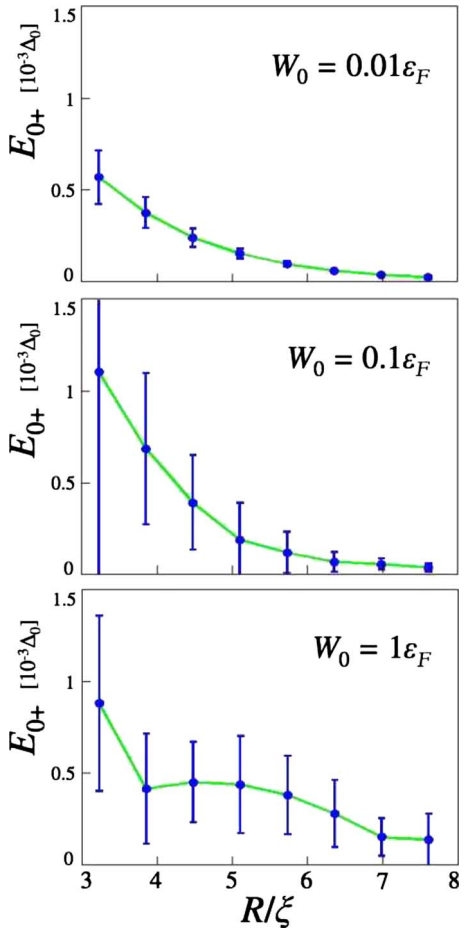

FIG. 8. (Color online) Disorder averaged energy of Majorana state E_{0+} versus R/ξ for increasing disorder strength W_0 (from top to bottom). The exponential decay survives in the regime $W_0 < \epsilon_F$.

Thus we conclude that the exponential drop of the Majorana state energy with increasing system size survives moderate disorder.

IV. SYSTEM WITH AN EDGE

The p_x+ip_y state has broken time-reversal symmetry, implying there are chiral modes which are exponentially localized at the edge of the sample. For a disk of radius R, the energies of the edge states are expected to have the form $E_m^{\text{edge}} \propto m/R$, where the angular momentum m is a half integer due to the antiperiodic boundary condition of the spin-polarized fermions.[8,26]

In the presence of a half-quantum vortex, the boundary condition on the BdG wave functions is periodic, and m is an integer, with the Majorana state having the $m=0$ quantum number. A fermion occupation number state is created from a combination of Majorana state on the edge and in the vortex core. This was recently investigated numerically.[27]

In order to create an edge at latitude θ_E, we add a strong potential of the form

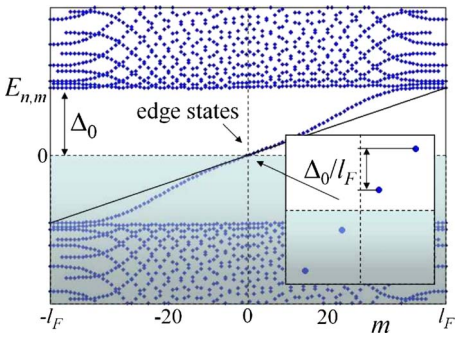

FIG. 9. (Color online) BdG spectrum $E_{n,m}$, of an edge without a vortex, depicting edge states. The solid black line is $m\Delta_0/l_F$. Here $R/\xi=7.6$, while the fit improves for larger R/ξ.

$$W_E(\theta) = \frac{2\epsilon_F}{e^{(\theta_E-\theta)2R/\xi}+1} = \sum_L w_L^E Y_{L0}(\mathbf{\Omega}), \tag{32}$$

which defines w_L^E. Note that at the edge $W_E(\theta_E)=\epsilon_F$, which sets the density to zero. The width of the potential was chosen to be the longer length scale ξ.

For a uniform superconductor with an edge, the order parameter is of the form

$$\Delta_E(\mathbf{\Omega},\mathbf{\Omega}') = \Delta_p(\mathbf{\Omega},\mathbf{\Omega}')F_E(\overline{\mathbf{\Omega}}), \tag{33}$$

$$F_E(\theta) = \begin{cases} \tanh[(\theta_E-\theta)R/\xi] & 0 \le \theta \le \theta_E \\ 0 & \theta_E \le \theta \le \pi \end{cases} = \sum_L f_L^E Y_{L0}(\mathbf{\Omega}), \tag{34}$$

where the pairing $\Delta_p(\mathbf{\Omega},\mathbf{\Omega}')$ is defined in Eq. (7) and the envelope $F_E(\overline{\mathbf{\Omega}})$ equals to zero for $\theta_E \le \theta \le \pi$ due to self-consistency. The matrix elements of W_E and Δ_E appear in Appendix C, which also shows that m is a good quantum number.

Figure 9 depicts the BdG spectrum of an edge without a vortex. The states above the gap $|E_n| > \Delta_0$ are extended, while the branch is composed of the chiral edge state. However, since there is only a single edge, these states are not degenerate.

In a half-infinite plane the dispersion of the edge states is given by[26] $E_{\mathbf{k}}^{\text{edge}} \approx \Delta_0 \frac{k}{k_F}$ with the velocity $v_{\text{edge}} = \frac{\Delta_0}{k_F}$. Conversion to spherical geometry with $R \gg \xi$ gives

$$E_m^{\text{edge}} \approx \Delta_0 \frac{m}{l_F}. \tag{35}$$

The black line in Fig. 9 depicts this approximation for $R/\xi = 7.6$. The approximation improves for larger values of R/ξ. Moreover, Fig. 10 shows that $E_m^{\text{edge}} \propto 1/R$, as expected.

When considering the antivortex in the north pole, the potential remains the same, while the order parameter becomes

$$\Delta_{\text{VE}}(\mathbf{\Omega},\mathbf{\Omega}') = \Delta_p(\mathbf{\Omega},\mathbf{\Omega}')F_{\text{VE}}(\overline{\mathbf{\Omega}}), \tag{36}$$

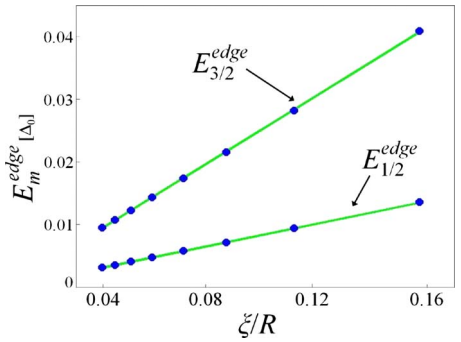

FIG. 10. (Color online) Energies of the two lowest edge states without a vortex E_m^{edge}, for $m=\frac{1}{2}$ and $m=\frac{3}{2}$, versus ξ/R, show the $1/R$ decay.

$$F_{\text{VE}}(\theta) = e^{i\phi}\begin{cases}\tanh\left[\sin\left(\pi\dfrac{\theta}{\theta_E}\right)\dfrac{R}{\xi}\right] & 0 \le \theta \le \theta_E \\ 0 & \theta_E \le \theta \le \pi\end{cases}$$
$$= \sum_L f_L^{\text{VE}} Y_{L1}(\mathbf{\Omega}). \tag{37}$$

Note that the vortex envelope F_{VE} is no longer symmetric with respect to the equator, and so includes $f_L^{\text{VE}} \neq 0$ for even L's, unlike F_V [Eq. (A14)]. The matrix elements of Δ_{VE} appear in Appendix C.

The resultant BdG spectrum, $E_{n,m}$, is shown in Fig. 11. The edge states and CdGM states appear in two separate branches. The only quasidegenerate state is the Majorana state at $m=\frac{1}{2}$.

Figure 12 depicts the wave functions of the Majorana state $u_{0^+}(\theta)$, the first excited edge state $u_{3/2}^{\text{edge}}(\theta)$ at $m=\frac{3}{2}$, and the first excited CdGM state $u_{-1/2}^{c}(\theta)$ at $m=-\frac{1}{2}$. It can be seen that the Majorana state has almost equal support on the edge and in the vortex core (and is exponentially localized in both), while the edge state and the CdGM state are concentrated *either* at the edge *or* at the vortex core, respectively. Figure 13 confirms that as expected the energy of the Majorana state E_{0^+} decays to zero as $e^{-R/\xi}$, while the energy of the first excited edge state $E_{3/2}^{\text{edge}}$ scales as $1/R$.

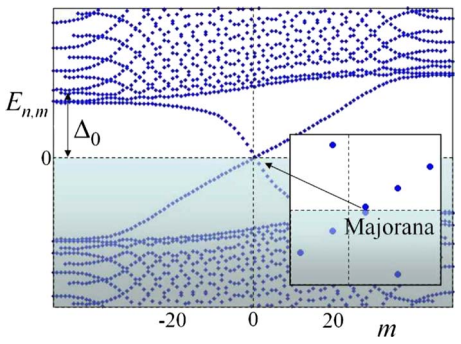

FIG. 11. (Color online) BdG spectrum $E_{n,m}$, of an antivortex with an edge, showing both the edge states and CdGM states. The Majorana state is present, with an exponentially small energy, as seen in the inset.

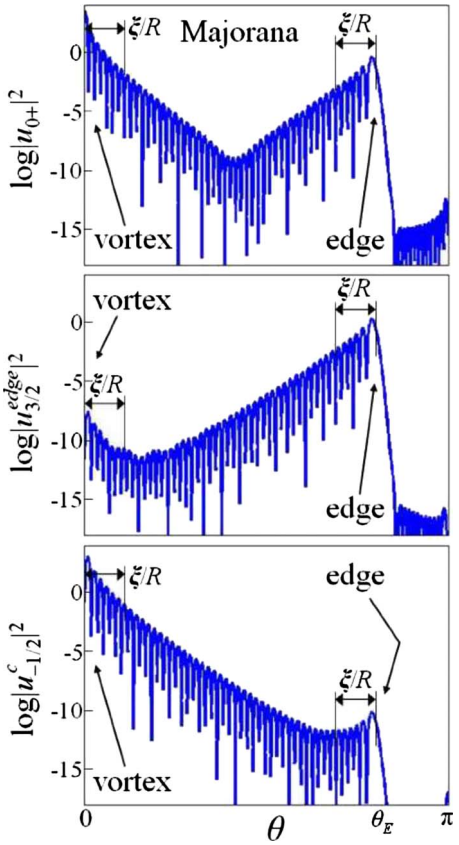

FIG. 12. (Color online) $\log|u(\theta)|^2$ of the Majorana state u_{0^+} (top), the first excited edge state $u_{3/2}^{\text{edge}}$ (middle), and the first excited CdGM state $u_{-1/2}^{c}$ (bottom). The Majorana state is split between the edge and the vortex core, while in each branch of excitation the wave function is concentrated either in edge *or* in the vortex core.

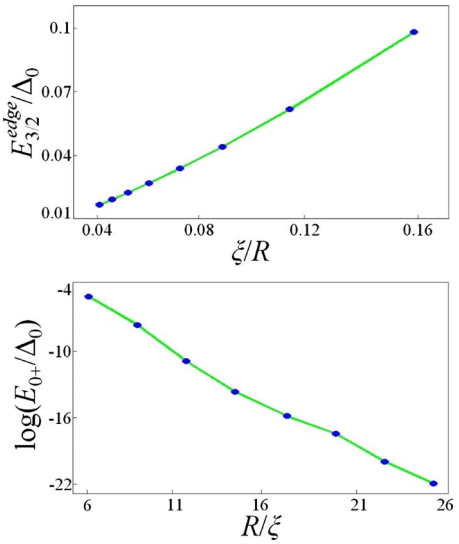

FIG. 13. (Color online) Energies of Majorana state E_{0^+} (bottom) and first excited edge state $E_{3/2}^{\text{edge}}$ (top) of an antivortex with an edge as a function of the radius of sphere R. The energy of the Majorana state decays exponentially, while the energy of the edge state scales as $1/R$.

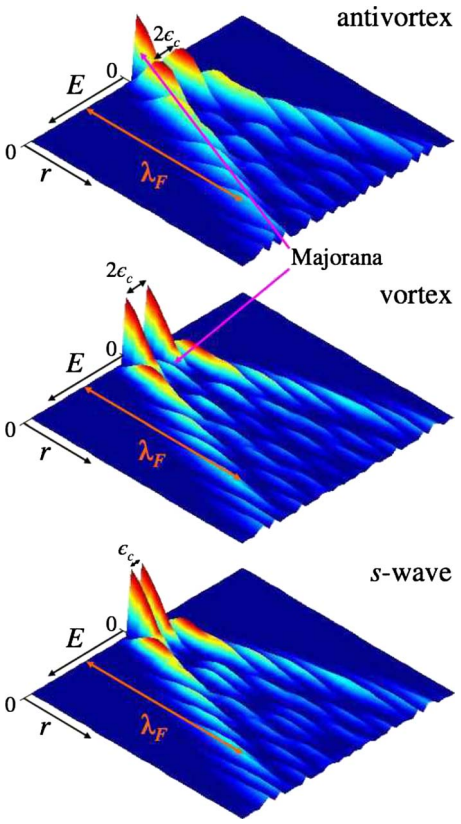

FIG. 14. (Color online) Zero-temperature LDOS $\mathcal{T}(E,r)$, in the cores of the p_x+ip_y antivortex (top) and vortex (middle), and of the s-wave vortex (bottom). ϵ_c is the spacing between CdGM states, and λ_F is the Fermi wavelength. The peaks belong to the CdGM states. Notice that the zero energy Majorana state is maximized at the origin in the p_x+ip_y antivortex, while it is removed from the origin in the vortex, and is absent in the s-wave.

In summary, the spherical geometry enables an easy visualization of edge effects by the addition of a confining potential. The expected edge states appear in any case, while the Majorana state appears only in the presence of a vortex.

V. TUNNELING LOCAL DENSITY OF STATES

The energy gap and the coherence length of a superconductor can be detected by tunneling of electrons to its surface. For high spatial resolution, the tunneling also detects the low-energy excitation spectrum inside a vortex core. In this section we show that tunneling experiment also provides direct signatures of the symmetry of the order parameter and the existence of the Majorana state.

At zero-temperature the tunneling local density of states (LDOS) is defined as[13]

$$\mathcal{T}(E,r) = \sum_n |u_n(r)|^2 \delta(E-E_n) + |v_n(r)|^2 \delta(E+E_n), \quad (38)$$

where r is the distance from the vortex (or antivortex) center. Figure 14 shows the LDOS at the core for displacements $r \leq 0.3\xi$ and energies $|E| \leq 0.2\Delta_0$. The p_x+ip_y state shows a distinction between the antivortex and the vortex, while in the s-wave they are the same.

The Majorana state can be easily discerned as zero energy peaks near the centers of the vortex and antivortex cores of the p_x+ip_y superconductor. The other CdGM core states also appear as oscillatory peaks, with energy spacing ϵ_c. The difference between the vortex and antivortex of the p_x+ip_y LDOS is apparent: according to Eq. (19) the antivortex Majorana state wave function behaves like J_0, which is peaked at $r=0$. By contrast, the vortex Majorana state wave function behaves like J_1, which is zero at $r=0$, and has a smaller peak at $r \approx \lambda_F/4$, where $\lambda_F = 2\pi/k_F$ is the Fermi wavelength.

The origin of this distinction was discussed in Sec. II. According to that argument, in the antivortex only the wave function of the Majorana state, with $m=\frac{1}{2}$, is real and peaked at the origin. All the excitations with $m \neq \frac{1}{2}$ have a phase winding, and are therefore equal to zero at the center of the vortex, and have much lower peaks. On the other hand, in the vortex the Majorana state wave function has a phase winding of $e^{i\phi}$, and must vanish at the origin. But the $u_m(\boldsymbol{x})$ part of the first excited state, with $m=-\frac{1}{2}$ and $E^c_{1/2}=\epsilon_c$, is real and finite at the center of the vortex. Similarly the $v_m(\boldsymbol{x})$ part of its negative companion, with $m=\frac{3}{2}$ and $E^c_{3/2}=-\epsilon_c$, is also real and finite at the center of the vortex. Therefore in the LDOS the first two excitations have relatively large peaks at $r=0$, while all the other CdGM states are much lower, as seen in Fig. 14.

The same argument holds for the s-wave superconductor. The phase winding of the order parameter with a vortex is $e^{i\phi}$, while with an antivortex it is $e^{-i\phi}$. This sign of the phase winding is only a matter of convention; there is no distinction in the s-wave superconductor between the vortex and the antivortex. Physically speaking, the pairing of the particles does not involve any internal angular momentum, so the sign of the vorticity is meaningless. For such an order parameter there is no Majorana fermion solution since it requires $u_0(\boldsymbol{x})=\tilde{u}_0(r)e^{i\phi/2}$, which is not single valued. However, for the lowest state, with $m=0$ and $E^c_0=\frac{1}{2}\epsilon_c$, $u_m(\boldsymbol{x})$ is real. Similarly $v_m(\boldsymbol{x})$ is real for $m=1$ (and $E^c_1=-\frac{1}{2}\epsilon_c$). Therefore, the two lowest states are peaked at the origin, while all the higher excitations are equal to zero at the origin, and therefore much lower, in agreement with Fig. 14.

In a tunneling spectroscopy experiment (e.g., Ref. 28), the tunneling conductance is measured. The conductance reflects the smearing of the LDOS by temperature broadening[29]

$$\frac{dI}{dV}(E,r) \sim T\int dE' \left(\frac{\partial f(E-E')}{\partial E'}\right)\mathcal{T}(E',r), \quad (39)$$

where $f(E)$ is the Fermi-Dirac distribution at zero chemical potential and temperature T. In the BCS weak-coupling regime, $\Delta_0 \ll \epsilon_F$, and therefore ϵ_c could be a very small temperature scale. At moderate temperatures $\epsilon_c < T < \Delta_0$, the peaks of Fig. 14 are smeared on the energy axis (but not on the r axis).

The tunneling conductance at $T=0.15\Delta_0=7.5\epsilon_c$, for displacements $r \leq \xi$ and energies $|E| \leq 1.5\Delta_0$, is depicted in Fig. 15 for the p_x+ip_y antivortex and vortex and for the s-wave

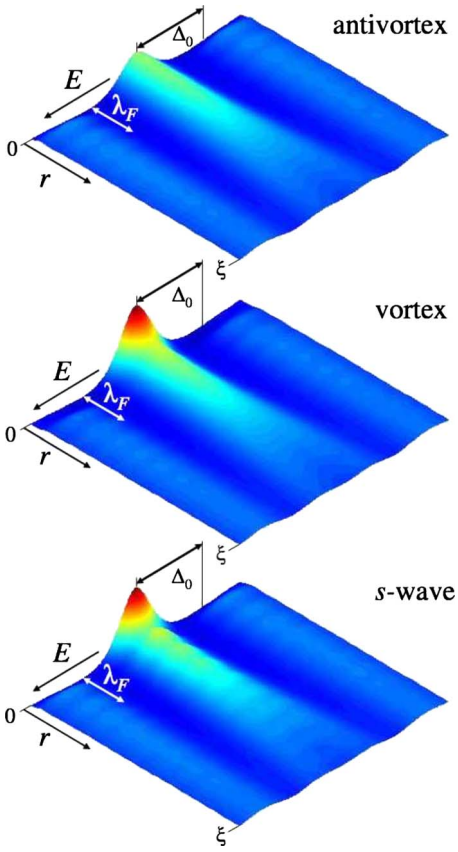

FIG. 15. (Color online) Tunneling conductance $\frac{dI}{dV}(E,r)$, in arbitrary units, of the p_x+ip_y antivortex (top) and vortex (middle), and of the s-wave vortex (bottom). Δ_0 is the energy gap, and ξ is the coherence length, which specifies the radiuses of the cores. The temperature $T=0.15\Delta_0$, is about 10 times larger than the CdGM level spacing. The conductance of the p_x+ip_y vortex is almost identical to that of the s-wave, while the central peak of the antivortex is twice lower.

vortex. The conductance shows a central peak at $E=0$, $r=0$, with low broad ridges dispersing away to larger E,r. We see that while the conductance of the p_x+ip_y vortex is almost identical to the conductance of the s-wave vortex, the central peak of the antivortex is half the height of that of the vortex.

The explanation for this factor of 2 comes from the origin of the zero-bias peak of the conductance. Consider the conductance of the s-wave vortex. Since this lacks a zero energy CdGM state, the zero-bias conductance vanishes at $T \ll \epsilon_c$. When the temperature is raised to $\frac{1}{2}\epsilon_c$, the two lowest CdGM states, which are peaked at the origin for $E \approx \pm \frac{1}{2}\epsilon_c$, broaden to create a zero-bias peak. As the temperature rises further, this peak diminishes due to the broadening, as shown by the blue curve of Fig. 16.

The p_x+ip_y vortex behaves similarly to the s-wave case, as shown by the green curve of Fig. 16. For $T \ll \epsilon_c$ the zero-bias conductance peak vanishes since the Majorana state wave function has a node at the origin. By contrast, for $T \geq \epsilon_c$ a zero-bias peak is created by the two broadened first excited states, which are peaked at the origin with $E \approx \pm \epsilon_c$. On the other hand, in the antivortex the Majorana state wave

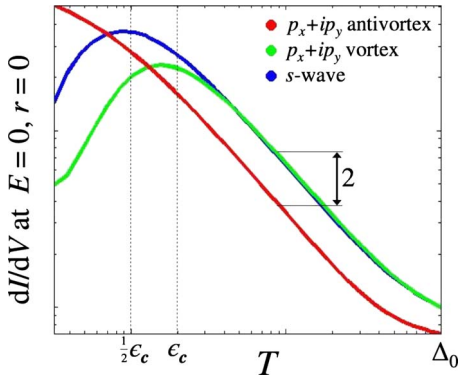

FIG. 16. (Color online) Zero-bias conductance peak at the (anti)vortex core as a function of temperature T in log-log scale. For $\epsilon_c < T < \Delta_0$ the p_x+ip_y vortex (green) and s-wave (blue) peaks are twice the height of the antivortex peak (red).

function is peaked exactly at the origin. Therefore its conductance is maximal at $T=0$ and diminishes with rising temperature, as depicted by the red curve of Fig. 16. Furthermore, since in the antivortex *only* the Majorana state is peaked at the origin, the height of the zero-bias peak of the antivortex is determined by *the broadening of a single state*, while in the vortex and in the s-wave it is *a sum of the broadening of two states*. This is why the central peak in the antivortex is half the height of that found in the vortex when $\epsilon_c < T < \Delta_0$. Thus, the asymmetry between the vortex and the antivortex is not only a clear fingerprint of the p_x+ip_y symmetry of the order parameter, but it is also a smoking gun evidence of the existence of the Majorana state itself.

The distinction between the vortex and the antivortex spectra is based on the distinction between the wave functions, which may be seen on scale of the Fermi wavelength λ_F. Therefore, as long as the spatial resolution in the tunneling conductance δr is better than λ_F, our effect is observable. But when $\frac{dI}{dV}(E,r)$ [Eq. (39)] is smeared over a length scale $(\delta r)^2 > \lambda_F^2$, the ratio between the vortex and antivortex peak heights rapidly approaches unity as $\delta r > \lambda_F$, as shown in Fig. 17. The requirement of such a high resolution, in spite of being restrictive, is feasible in present technology of $\delta r \approx 1$ Å since in Sr_2RuO_4 $\lambda_F \approx 8.3$ Å.[30]

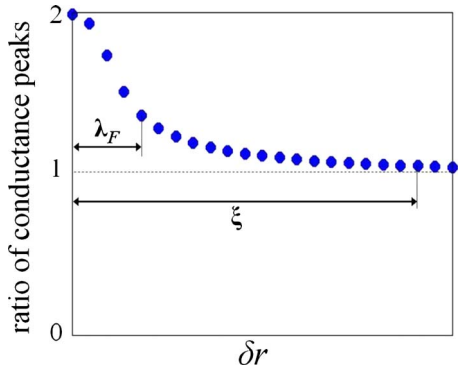

FIG. 17. (Color online) Effect of spatial resolution. Ratio of vortex to antivortex conductance peak heights (shown in Fig. 16 for perfect resolution) for spatial resolution δr. λ_F and ξ are Fermi wavelength and coherence lengths, respectively. Temperature is $7.5\epsilon_c$.

Moreover, although we found in Sec. III that the Majorana state survives moderate disorder, the suggested results hold provided the disorder is weak on the scale of λ_F, which is very reasonable as that limit corresponds to minimum conductivity and Anderson localization.

The above analysis is based on the two dimensionality of the sample. In real three-dimensional samples the conductance peaks are strongly suppressed by bulk states and surface imperfections.[28,31] Nevertheless, it is the *difference* between a vortex peak and an antivortex peak which is sensitive to the existence of the Majorana state. Moreover, according to the asymptotic analysis,[16] momentum along the vortex line (additional $e^{ik_z z}$ in the wave function) leaves the dispersion of the core states [Eq. (18)] unchanged and only modifies weakly the oscillations in the radial part of the wave function (through the oscillatory argument, which becomes $\sqrt{k_F^2+k_z^2}r$).

Performing such an experiment is certain to be a challenge although likely remains possible. One might imagine leaving the tip of the STM in the same position while reversing a weak magnetic field where the field is weak enough so as to flip the direction of the vortex but not to overturn the chiral order parameter. Such an experiment would rely on an assumption that the vortex prefers to sit at one particular position in the sample—presumably due to some inhomogeneity or disorder in the sample—and that this preferred position does not change when the weak magnetic field is reversed. In practice, however, one would have to check this assumption by spatially scanning the STM as even a small change in the vortex position would have a large effect on the measured tunneling.

General Cases. A difference between vortex and antivortex conductance peak is expected for any chiral symmetry-breaking (CSB) superconductor. The important questions are whether this difference is observable for $T>\epsilon_c$ and whether it is sensitive to the existence of Majorana fermions.

For a CSB superconductor with relative angular momentum $M=1,2,\ldots$ (chiral-p, chiral-d,…), in the presence of a vortex with vorticity $N=\pm 1,\pm 2,\ldots$, the phase winding of the order parameter is $e^{i(M+N)\phi}$. A Majorana fermion solution $u_0 \sim e^{im\phi}$ requires $m=(M+N)/2$ and would be single valued only if m is an integer, i.e., $M+N$ is even. However, only if $M+N=0$ can the wave function of the Majorana state be finite at the center of the vortex, i.e., an antivortex with vorticity $N=-M$. Therefore, although a Majorana state is expected for every even $M+N$,[9] the asymmetry in the zero-bias conductance peak for $T>\epsilon_c$ is expected only in the subset $|N|=M$. Notice that the p_x+ip_y vortex is the only case where the asymmetry occurs for a unit vorticity.

VI. SUMMARY

Implementing the BdG equation of a p_x+ip_y superconductor on a sphere had several advantages. It allowed us to study the system with and without vortices and edges, without artifacts of finite-size boundaries. We found the exponential decay of the Majorana state energy with respect to the intervortex distance to be robust with respect to the addition of moderate disorder strength up to the Fermi energy scale. The tunneling conductance was plotted and compared to the s-wave case. It was found that in the moderate temperature regime $\epsilon_c<T<\Delta_0$, the zero-bias conductance in the center of the p_x+ip_y antivortex is half the height of that of the vortex. The asymmetry in the conductance peak heights is a smoking gun signature of the spin-polarized p_x+ip_y superconductor and a direct measurement of the existence of the Majorana state. This idea can be generalized to order parameters of higher angular momentum.

ACKNOWLEDGMENTS

We thank Ady Stern for useful discussions. Support from US-Israel Binational Science foundation and Israel Science foundation is acknowledged. A.A. acknowledges Aspen Center for Physics for its hospitality. H.A.F. acknowledges the support of the NSF through Grant No. DMR-0704033. A.A. and S.H.S. acknowledge the hospitality of the KITP, where this collaboration was initiated.

APPENDIX A: THE MATRIX ELEMENT $\Delta^V_{lm,l'm'}$

In this appendix we derive $\Delta^V_{lm,l'm'}$ [Eqs. (13) and (14)] from Δ_V [Eqs. (6)–(8)].

The spinor functions α and β [Eq. (8)] obey

$$\alpha\beta' - \beta\alpha' = 2\pi[Y_{-1/2,1/2,1/2}(\mathbf{\Omega})Y_{-1/2,1/2,-1/2}(\mathbf{\Omega}') - Y_{-1/2,1/2,-1/2}(\mathbf{\Omega})Y_{-1/2,1/2,1/2}(\mathbf{\Omega}')] \quad \text{(A1)}$$

and

$$\begin{aligned}|\alpha\alpha'^* + \beta\beta'^*|^{2(R/\xi_p)^2} &= \left|\cos\frac{\theta}{2}\cos\frac{\theta'}{2} + \sin\frac{\theta}{2}\sin\frac{\theta'}{2}e^{i(\phi-\phi')}\right|^{2(R/\xi_p)^2} \\ &= \left(\frac{1+\cos\theta\cos\theta'+\sin\theta\sin\theta'\cos(\phi-\phi')}{2}\right)^{(R/\xi_p)^2} \\ &= \left(\frac{1+\cos\Theta}{2}\right)^{(R/\xi_p)^2}, \end{aligned} \quad \text{(A2)}$$

where Θ is the angle between $\mathbf{\Omega}$ and $\mathbf{\Omega}'$. Note that for $\xi_p \ll R$

$$\left(\frac{1+\cos\Theta}{2}\right)^{(R/\xi_p)^2} \approx e^{-(R/\xi_p)^2\Theta^2/4}, \quad \text{(A3)}$$

which is equivalent to Gaussian pairing in the plane.

If we denote $M=[(R/\xi_p)^2]$, then

$$|\alpha\alpha'^* + \beta\beta'^*|^{2(R/\xi_p)^2} \approx \frac{1}{2^M}(1+\cos\Theta)^M = \frac{1}{2^M}\sum_{n=0}^{M}\binom{M}{n}\cos^n\Theta. \quad \text{(A4)}$$

Any monomial x^n can be expressed as a series of Legendre polynomials $P_l(x)$ (Ref. 32);

$$x^n = \sum_{l=n,n-2,\ldots}\frac{(2l+1)n!}{2^{(n-l)/2}\left(\frac{n-l}{2}\right)!\,(l+n+1)!!}P_l(x), \quad \text{(A5)}$$

which satisfy[33]

$$P_l(\cos\Theta) = \frac{4\pi}{2l+1}\sum_{m=-l}^{l}(-1)^m Y_{l-m}(\mathbf{\Omega})Y_{lm}(\mathbf{\Omega}'), \quad \text{(A6)}$$

where Y_{lm} (Y_{0lm}) are the spherical harmonics. Substituting Eqs. (A5) and (A6) into Eq. (A4), we obtain

$$|\alpha\alpha' + \beta\beta'|^{2(R/\xi_p)^2} \approx 4\pi\frac{M!}{2^M}\sum_{l=0}^{M}\sum_{m=-l}^{l}(-1)^m A_l^M Y_{l-m}(\mathbf{\Omega})Y_{lm}(\mathbf{\Omega}'),$$

$$A_l^M = \sum_{n=l,l+2,\ldots}^{M}\left[2^{(n-l)/2}\left(\frac{n-l}{2}\right)!\,(M-n)!\,(l+n+1)!!\right]^{-1}. \quad \text{(A7)}$$

Multiplying two harmonics yields[25]

$$Y_{qlm}(\mathbf{\Omega})Y_{q'l'm'}(\mathbf{\Omega}) = (-1)^{l+l'-q-q'-m-m'}\sqrt{\frac{1}{4\pi}(2l+1)(2l'+1)} \times \sum_{l''=|l-l'|}^{l+l'}(-1)^{l''}\sqrt{2l''+1}\begin{pmatrix} l & l' & l'' \\ m & m' & -m-m' \end{pmatrix} \times \begin{pmatrix} l & l' & l'' \\ q & q' & -q-q' \end{pmatrix} Y_{q+q',l'',m+m'}(\mathbf{\Omega}). \quad \text{(A8)}$$

In particular

$$\begin{aligned} Y_{0lm}(\mathbf{\Omega})Y_{-1/2,1/2,\pm 1/2}(\mathbf{\Omega}) &= (-1)^{m-1}\sqrt{\frac{1}{2\pi}(2l+1)} \times \sum_{s=\pm 1/2}(-1)^{s\mp 1/2}\sqrt{2l'+1\pm 2s} \\ &\times \begin{pmatrix} l & \frac{1}{2} & l+s \\ m & \pm\frac{1}{2} & -m\mp\frac{1}{2} \end{pmatrix} \times \begin{pmatrix} l & \frac{1}{2} & l+s \\ 0 & -\frac{1}{2} & \frac{1}{2} \end{pmatrix} Y_{-1/2,l+s,m\pm 1/2}(\mathbf{\Omega}) \\ &= \sqrt{\frac{1}{4\pi}}\left(\sqrt{\frac{l\pm m+1}{2l+1}}Y_{-1/2,l+1/2,m\pm 1/2}(\mathbf{\Omega}) \pm \sqrt{\frac{l\mp m+1}{2l+1}}Y_{-1/2,l-1/2,m\pm 1/2}(\mathbf{\Omega})\right), \end{aligned} \quad \text{(A9)}$$

where the last expression comes from writing the $3j$ symbols explicitly.[33]

Substituting Eqs. (A1), (A7), and (A9) into Eq. (7) yield

$$\begin{aligned} \Delta_p(\mathbf{\Omega},\mathbf{\Omega}') &= \frac{\Delta_0}{R^2}\frac{M^2\cdot M!}{2^{M+1}\left(l_F+\frac{1}{2}\right)}\sum_{l=0}^{M}(A_l^M - A_{l+1}^M) \\ &\times \sum_{m=-l-1}^{l}(-1)^{m+1}Y_{-1/2,l+1/2,-m-1/2}(\mathbf{\Omega}) \\ &\times Y_{-1/2,l+1/2,m+1/2}(\mathbf{\Omega}') \\ &= \frac{\Delta_0}{R^2}\sum_{l=1/2}^{M+1/2}D_l\sum_{m=-l}^{l}(-1)^{m-1/2}Y_{-1/2,l,m}(\mathbf{\Omega}) \\ &\times Y_{-1/2,l,-m}(\mathbf{\Omega}'), \end{aligned} \quad \text{(A10)}$$

with

$$D_l = \frac{M^2\cdot M!}{2^{M+1}\left(l_F+\frac{1}{2}\right)} \times \left\{B_l^M + \sum_{n=0,2,\ldots}^{M-l-1/2}\left(\frac{1}{M-l+\frac{1}{2}-n} - \frac{1}{2l+2+n}\right) \times \left[2^{n/2}\left(\frac{n}{2}\right)!\left(M-l-\frac{1}{2}-n\right)!\,(2l+n)!!\right]^{-1}\right\}, \quad \text{(A11)}$$

where $B_l^M = \{2^{1/2(M-l+1/2)}[\frac{1}{2}(M-l+\frac{1}{2})]!\,(M+l+\frac{1}{2})!!\}^{-1}$ only for $l-\frac{1}{2}\equiv M(\mathrm{mod}\ 2)$.

Alternatively, substituting $k_x+ik_y \to (l+\frac{1}{2})/R$ in the planar $\Delta_{\mathbf{k}}$ [Eq. (3)] yields an excellent approximation for D_l,

$$D_l \approx \frac{l+\frac{1}{2}}{l_F+\frac{1}{2}}e^{-(l+1/2)^2(\xi_p/R)^2}, \quad \text{(A12)}$$

which is valid for $R>5\xi_p$. For l, $l_F \gg 1$ we obtain Eq. (14).

For short-range pairing $\xi_p \ll R$, the vorticity of the center of mass can be approximated by

$$F_V(\overline{\mathbf{\Omega}}) \approx \tfrac{1}{2}[F_V(\mathbf{\Omega}) + F_V(\mathbf{\Omega}')]. \quad \text{(A13)}$$

F_V is expanded in spherical harmonics,

$$F_V(\mathbf{\Omega}) = \sum_{L=1,3,5,\ldots} f_L^V Y_{L1}(\mathbf{\Omega}), \quad \text{(A14)}$$

which defines f_L^V.

Substituting Eqs. (A10) and (A14) into Eq. (6) and using Eq. (A8) yield

$$\Delta_V(\mathbf{\Omega},\mathbf{\Omega}') = \frac{\Delta_0}{R^2}\sum_{\substack{lm\\ l'L}} (-1)^{l+l'+L} D_l \cdot f_L^V \sqrt{\frac{1}{16\pi}(2l+1)(2l'+1)(2L+1)} \begin{pmatrix} l & L & l' \\ -\frac{1}{2} & 0 & \frac{1}{2} \end{pmatrix}$$
$$\times \left[\begin{pmatrix} l & L & l' \\ -m & 1 & m-1 \end{pmatrix} Y_{-1/2,l,m}(\mathbf{\Omega}) Y_{-1/2,l',-m+1}(\mathbf{\Omega}') - \begin{pmatrix} l & L & l' \\ m & 1 & -m-1 \end{pmatrix} Y_{-1/2,l',m+1}(\mathbf{\Omega}) Y_{-1/2,l,-m}(\mathbf{\Omega}') \right]$$
$$= \frac{1}{R^2} \sum_{lml'm'} \Delta^V_{lm,l'm'} Y_{-1/2,l,m}(\mathbf{\Omega}) Y_{-1/2,l',m'}(\mathbf{\Omega}'). \tag{A15}$$

The last line defines $\Delta^V_{lm,l'm'}$. Finally, by using[33]

$$\begin{pmatrix} l & l' & l'' \\ m & m' & m'' \end{pmatrix} = \begin{pmatrix} l'' & l & l' \\ m'' & m & m' \end{pmatrix}$$
$$= (-1)^{l+l'+l''} \begin{pmatrix} l'' & l' & l \\ m'' & m' & m \end{pmatrix}$$
$$= (-1)^{l+l'+l''} \begin{pmatrix} l & l' & l'' \\ -m & -m' & -m'' \end{pmatrix}, \tag{A16}$$

we obtain

$$\Delta^V_{lm,l'm'} = \delta_{m',-m+1} \Delta_0 \sqrt{\frac{1}{16\pi}(2l+1)(2l'+1)}$$
$$\times \sum_L \sqrt{2L+1} f_L^V [D_l - (-1)^{l+l'+L} D_{l'}]$$
$$\times \begin{pmatrix} l & l' & L \\ \frac{1}{2} & -\frac{1}{2} & 0 \end{pmatrix} \begin{pmatrix} l & l' & L \\ -m & m-1 & 1 \end{pmatrix}. \tag{A17}$$

Since L is odd, we obtain Eq. (13). Note that $\Delta^V_{l,m,l',-m+1} = -\Delta^V_{l',-m+1,l,m}$, as expected by the antisymmetry.

APPENDIX B: THE DISORDER POTENTIAL

The white-noise potential is defined as a series of independently identically distributed complex elements w_{lm}, with both real and imaginary parts uniformly distributed in the interval $[-\frac{\sqrt{6\pi}W_0}{l_\Lambda}, \frac{\sqrt{6\pi}W_0}{l_\Lambda}]$ for every $l \le l_\Lambda$. Therefore

$$\langle w^*_{lm} w_{l'm'} \rangle = \delta_{ll'} \delta_{mm'} \langle |w_{lm}|^2 \rangle$$
$$= \delta_{ll'} \delta_{mm'} 2 \langle |\mathrm{Re}(w_{lm})|^2 \rangle$$
$$= \delta_{ll'} \delta_{mm'} \frac{4\pi}{l_\Lambda^2} W_0^2, \quad \forall\, l \le l_\Lambda. \tag{B1}$$

In real space

$$\langle W^2(\mathbf{\Omega}) \rangle = \sum_{\substack{l,m\\ l',m'}}^{l_\Lambda} \langle w^*_{lm} w_{l'm'} \rangle Y^*_{lm}(\mathbf{\Omega}) Y_{l'm'}(\mathbf{\Omega})$$
$$= W_0^2 \frac{4\pi}{l_\Lambda^2} \sum_{l,m}^{l_\Lambda} |Y_{lm}(\mathbf{\Omega})|^2. \tag{B2}$$

In particular for the north pole

$$\langle W^2(\theta=0) \rangle = W_0^2 \frac{4\pi}{l_\Lambda^2} \sum_{l=0}^{l_\Lambda} |Y_{l0}(\theta=0)|^2$$
$$= W_0^2 \frac{4\pi}{l_\Lambda^2} \sum_{l=0}^{l_\Lambda} \frac{2l_\Lambda+1}{4\pi} \approx W_0^2. \tag{B3}$$

In order to calculate the matrix element $W_{lm,l'm'}$, we use the identities[25]

$$Y^*_{qlm}(\mathbf{\Omega}) = (-1)^{q+m} Y_{-ql-m}(\mathbf{\Omega}), \tag{B4}$$

and

$$\int d\mathbf{\Omega} Y_{qlm}(\mathbf{\Omega}) Y_{q'l'm'}(\mathbf{\Omega}) Y_{q''l''m''}(\mathbf{\Omega})$$
$$= (-1)^{l+l'+l} \sqrt{\frac{1}{4\pi}(2l+1)(2l'+1)(2l''+1)}$$
$$\times \begin{pmatrix} l & l' & l'' \\ q & q' & q'' \end{pmatrix} \begin{pmatrix} l & l' & l'' \\ m & m' & m'' \end{pmatrix}. \tag{B5}$$

Hence

$$W_{lm,l'm'} = \int d\mathbf{\Omega} Y^*_{-1/2,l,m}(\mathbf{\Omega}) W(\mathbf{\Omega}) Y_{-1/2,l',m'}(\mathbf{\Omega})$$
$$= (-1)^{m-1/2} \sum_{l'',m''} w_{l''m''} \int d\mathbf{\Omega} Y_{1/2,l,-m}(\mathbf{\Omega})$$
$$\times Y_{-1/2,l',m'}(\mathbf{\Omega}) Y_{0l''m''}(\mathbf{\Omega}), \tag{B6}$$

which yields Eq. (31). Note that $W_{l'm',lm} = W^*_{lm,l'm'}$, as expected from a real potential.

APPENDIX C: MATRIX ELEMENTS OF EDGE OPERATORS

Both the edge potential operator W_E [Eq. (32)] and order parameter Δ_E [Eq. (33)] have the following matrix elements:

$$W^E_{lm,l'm'} = \delta_{m',-m}(-1)^{m-1/2}\sqrt{\frac{1}{4\pi}(2l+1)(2l'+1)} \times \sum_L \sqrt{2L+1} w^E_L \begin{pmatrix} l & l' & L \\ \frac{1}{2} & -\frac{1}{2} & 0 \end{pmatrix} \begin{pmatrix} l & l' & L \\ m & -m & 0 \end{pmatrix}, \tag{C1}$$

$$\Delta^E_{lm,l'm'} = \delta_{m',-m}\Delta_0\sqrt{\frac{1}{16\pi}(2l+1)(2l'+1)} \times \sum_L \sqrt{2L+1} f^E_L [D_{l'} - (-1)^{l+l'+L} D_l] \times \begin{pmatrix} l & l' & L \\ \frac{1}{2} & -\frac{1}{2} & 0 \end{pmatrix} \begin{pmatrix} l & l' & L \\ m & -m & 0 \end{pmatrix}. \tag{C2}$$

$W^E_{lm,l'm'}$ is obtained by substituting $m=m'$ in Eq. (31) [due to Eq. (32)]. $\Delta^E_{lm,l'm'}$ is essentially Eq. (A17). But since F_E [Eq. (34)] replaces F_V [Eq. (A14)], m is coupled to $-m$, and $f^E_L \neq 0$ for both odd and even L's.

For the case of an edge with a vortex, the matrix elements of the order parameter Δ_{VE} [Eq. (36)] are

$$\Delta^{\mathrm{VE}}_{lm,l'm'} = \delta_{m',-m+1}\Delta_0\sqrt{\frac{1}{16\pi}(2l+1)(2l'+1)} \times \sum_L \sqrt{2L+1} f^{\mathrm{VE}}_L [D_l - (-1)^{l+l'+L} D'_l] \times \begin{pmatrix} l & l' & L \\ \frac{1}{2} & -\frac{1}{2} & 0 \end{pmatrix} \begin{pmatrix} l & l' & L \\ -m & m-1 & 1 \end{pmatrix}, \tag{C3}$$

which are exactly Eq. (A17), with $f^{\mathrm{VE}}_L \neq 0$ for both odd and even L's.

[1] C. Nayak, S. H. Simon, A. Stern, M. Freedman, and S. Das Sarma, Rev. Mod. Phys. **80**, 1083 (2008).

[2] While such systems are not universal for topological quantum computation, they could serve as quantum memories. Schemes have also been constructed for partially topological quantum computation. See S. Bravyi, Phys. Rev. A **73**, 042313 (2006).

[3] G. E. Volovik, *The Universe in a Helium Droplet* (Clarendon Press, Oxford, 2003).

[4] T. M. Rice and M. Sigrist, J. Phys.: Condens. Matter **7**, L643 (1995); G. Baskaran, Physica B **223-224**, 490 (1996); Y. Maeno, T. M. Rice and M. Sigrist, Phys. Today **54**(1), 42 (2001).

[5] G. Moore and N. Read, Nucl. Phys. B **360**, 362 (1991).

[6] M. Greiter, X. G. Wen, and F. Wilczek, Nucl. Phys. B **374**, 567 (1992).

[7] V. Gurarie and L. Radzihovsky, Ann. Phys. **322**, 2 (2007).

[8] N. Read and D. Green, Phys. Rev. B **61**, 10267 (2000).

[9] G. E. Volovik, Pis'ma Zh. Eksp. Teor. Fiz. **70**, 601 (1999) [JETP Lett. **70**, 609 (1999)].

[10] In Sr_2RuO_4, the "full-quantum vortex" (a vortex in the order parameter of both spin components) has lower energy than the half-quantum vortex so that the half-quantum vortex does not naturally occur. Nonetheless, several proposals have appeared for how to stabilize the half-quantum vortices. See S. Das Sarma, C. Nayak, and S. Tewari, Phys. Rev. B **73**, 220502(R) (2006); S. B. Chung, H. Bluhm, and E.-A. Kim, Phys. Rev. Lett. **99**, 197002 (2007); In ^{3}HeA, see M. M. Salomaa and G. E. Volovik, *ibid.* **55**, 1184 (1985).

[11] For the 5/2 state there are now several experiments that claim to observe the $e/4$ quasiparticle, which would be the Majorana fermion carrying vortex. See M. Dolev, M. Heiblum, V. Umansky, Ady Stern, and D. Mahalu, Nature (London) **452**, 829 (2008); I. P. Radu, J. B. Miller, C. M. Marcus, M. A. Kastner, L. N. Pfeiffer, and K. W. West, Science **320**, 899 (2008); R. L. Willett, M. J. Manfra, L. N. Pfeiffer, and K. W. West, arXiv:0807.0221 (unpublished).

[12] Proposals based on tunneling of the Majorana state between two vortices were given by C. J. Bolech and E. Demler, Phys. Rev. Lett. **98**, 237002 (2007); S. Tewari, C. Zhang, S. Das Sarma, C. Nayak, and D. H. Lee, *ibid.* **100**, 027001 (2008).

[13] J. D. Shore, M. Huang, A. T. Dorsey, and J. P. Sethna, Phys. Rev. Lett. **62**, 3089 (1989).

[14] For ^{3}HeA one can at least imagine tunneling an atom through a nanoconstriction at varying pressure although in practice this might be extremely difficult. For the 5/2 state, tunneling in or out of the system requires flux-attachment (see Ref. 8) and would likely result in a strong pseudogap in the tunneling amplitude. See, for example, S. He, P. M. Platzman, and B. I. Halperin, Phys. Rev. Lett. **71**, 777 (1993).

[15] C. Caroli, P. G. de Gennes, and J. Matricon, Phys. Lett. **9**, 307 (1964).

[16] N. B. Kopnin and M. M. Salomaa, Phys. Rev. B **44**, 9667 (1991).

[17] Sr_2RuO_4 has shown breaking of time-reversal symmetry, see G. M. Luke, Y. Fudamoto, K. M. Kojima, M. I. Larkin, J. Merrin, B. Nachumi, Y. J. Uemura, Y. Maeno, Z. Q. Mao, Y. Mori, H. Nakamura, and M. Sigrist, Nature (London) **394**, 558 (1998).

[18] For additional vortex-antivortex asymmetry, see T. Yokoyama, C. Iniotakis, Y. Tanaka, and M. Sigrist, Phys. Rev. Lett. **100**, 177002 (2008); M. A. Silaev, T. Yokoyama, J. Linder, Y. Tanaka, and A. Sudbø, Phys. Rev. B **79**, 054508 (2009).

[19] A. Auerbach, D. P. Arovas, and S. Ghosh, Phys. Rev. B **74**, 064511 (2006).

[20] Y. E. Kraus, A. Auerbach, H. A. Fertig, and S. H. Simon, Phys. Rev. Lett. **101**, 267002 (2008).

[21] P. G. de Gennes, *Superconductivity of Metals and Alloys* (WA Benjamin Inc., New York, 1966).
[22] M. Tinkham, *Introduction to Superconductivity* (Krieger, New York, 1980).
[23] J. K. Jain and R. K. Kamilla, Phys. Rev. B **55**, R4895 (1997); G. Moller and S. H. Simon, *ibid.* **77**, 075319 (2008).
[24] C. Pethik and H. Smith, *Bose Einstein Condensation in Dilute Gases* (Cambridge University Press, Cambridge, 2002).
[25] T. T. Wu and C. N. Yang, Nucl. Phys. B **107**, 365 (1976); Phys. Rev. D **16**, 1018 (1977).
[26] P. Fendley, M. P. A. Fisher, and C. Nayak, Phys. Rev. B **75**, 045317 (2007).
[27] Y. Tsutsumi, T. Kawakami, T. Mizushima, M. Ichioka, and K. Machida, Phys. Rev. Lett. **101**, 135302 (2008); T. Mizushima, M. Ichioka, and K. Machida, *ibid.* **101**, 150409 (2008).
[28] C. Lupien, S. K. Dutta, B. I. Barker, Y. Maeno, and J. C. Davis, arXiv:cond-mat/0503317 (unpublished).
[29] F. Gygi and M. Schlüter, Phys. Rev. B **41**, 822 (1990); **43**, 7609 (1991).
[30] A. P. Mackenzie and Y. Maeno, Rev. Mod. Phys. **75**, 657 (2003).
[31] H. F. Hess, R. B. Robinson, R. C. Dynes, J. M. Valles, and J. V. Waszczak, Phys. Rev. Lett. **62**, 214 (1989).
[32] M. Abramowitz and I. A. Stegun, *Handbook of Mathematical Functions* (Dover, New York, 1972).
[33] A. R. Edmonds, *Angular Momentum in Quantum Mechanics* (Princeton University Press, Princeton, 1960).